Terr. Atmos. Ocean. Sci., Vol. 32, No. 2, 217-228, April 2021 doi: 10.3319/TAO.2021.03.30.01

Modeling the disappearance of equatorial plasma bubble by nighttime medium-scale traveling ionospheric disturbances

Min-Yang Chou[1, *], Charles C. H. Lin[2], and Joseph D. Huba[3]

[1] *COSMIC Program Office, University Corporation for Atmospheric Research, Boulder, CO, USA*
[2] *Department of Earth Sciences, National Cheng Kung University, Tainan City, Taiwan*
[3] *Syntek Technologies, Fairfax, VA, USA*

Article history:
Received 26 February 2021
Revised 17 April 2021
Accepted 30 March 2021

Keywords:
Equatorial plasma bubbles, Nighttime MSTIDs, Numerical simulations, Disappearance of EPBs

Citation:
Chou, M.-Y., C. C. H. Lin, and J. D. Huba, 2021: Modeling the disappearance of equatorial plasma bubble by nighttime medium-scale traveling ionospheric disturbances. Terr. Atmos. Ocean. Sci., 32, 217-228, doi: 10.3319/TAO.2021.03.30.01

ABSTRACT

The Naval Research Laboratory first-principles ionosphere model SAMI3/ESF is performed to study the interaction between the nighttime medium-scale traveling ionospheric disturbances (MSTIDs) and equatorial plasma bubbles (EPBs). The synthetic dynamo currents are imposed into the potential equation to induce polarization electric fields for generating the MSTIDs. Simulations demonstrate that the MSTIDs can inhibit the upward growth of EPBs; however, MSTIDs alone are insufficient to explain the disappearance of EPBs. We found that the meridional winds likely contribute to the disappearance of MSTIDs by reducing the background electron density and polarization electric fields within the EPBs. Then, the MSTIDs transport plasma to fill the EPB depletions up via $\mathbf{E} \times \mathbf{B}$ drifts. Both MSTIDs and meridional winds are necessary to comprehend the underlying mechanism of EPB disappearance. Additionally, we also found that the zonal and vertical $\mathbf{E} \times \mathbf{B}$ drifts within the MSTIDs affect the morphology of EPBs, leading to a reverse-C shape structure.

1. INTRODUCTION

Ionospheric irregularities associated with equatorial plasma bubbles (EPBs) and nighttime medium-scale traveling ionospheric disturbances (MSTIDs) are often observed in the nighttime equatorial and mid-latitude ionosphere. They are electrodynamical structures generated by the generalized Rayleigh-Taylor instability (e.g., Kelley 1989) and Perkins instability (Perkins 1973), respectively. Dungey (1956) first proposed the Rayleigh-Taylor instability as the mechanism responsible for driving EPBs. The low-density plasma moves upward into the high-density plasma region via $\mathbf{E} \times \mathbf{B}$ drifts driven by gravitational force-induced ion currents, creating ionospheric plasma depletions along magnetic flux tubes. The meridionally-elongated wedges of plasma depletions displaying geomagnetic conjugacy have been observed by ground- and space-based airglow imagers (Otsuka et al. 2002; Ogawa et al. 2005). Various seeding mechanisms have been proposed to explain the generation of EPBs, such as the neutral winds, gravity waves, and electric and magnetic fields (Sultan 1996; Rama Rao et al. 1997; Abdu et al. 2009; Li et al. 2016). The pre-reversal enhancement (PRE) is considered to play a dominant role in causing the post-sunset rise of the ionospheric layer, resulting in the steep vertical gradient of electron density favorable for the development of EPBs (e.g., Tulasi Ram et al. 2006, 2007; Rajesh et al. 2017).

On the other hand, the nighttime MSTIDs have been investigated for many years (e.g., Behnke 1979; Miller et al. 1997; Saito et al. 1998; Shiokawa et al. 2003a; Rajesh et al. 2016; Chou et al. 2017). Space- and ground-based observations have shown the oscillation of polarization electric fields within the MSTIDs (Saito et al. 1995; Kelley et al. 2000; Shiokawa et al. 2003b), supporting the hypothesis that the Perkins instability plays a crucial role in the generation of MSTIDs. The polarization electric fields can further map along the geomagnetic field lines, displaying conjugate

* *Corresponding author*
E-mail: chou@ucar.edu

structures in both hemispheres (Otsuka et al. 2004). Since the theoretical growth rate of the Perkins instability is quite small, gravity wave seeding (Kelley and Fukao 1991; Huang et al. 1994; Miller et al. 1997; Chou et al. 2017, 2018) or coupling between the F and sporadic-E layers (EsL) (Cosgrove and Tsunoda 2004; Tsunoda et al. 2004; Yokoyama et al. 2009) are suggested to be the plausible mechanisms to accelerate the growth of nighttime MSTIDs.

Earlier studies have reported the interaction between EPBs and MSTIDs. MSTIDs can be one of the seeding mechanisms to trigger EPBs (Miller et al. 2009; Krall et al. 2011; Takahashi et al. 2018). Krall et al. (2011) suggested that the coupling between the MSTIDs and the equatorial ionosphere can lead to the growth of EPBs. Interestingly, some other studies have reported that MSTIDs can suppress or aid the extension of EPBs (Otsuka et al. 2012; Shiokawa et al. 2015; Aa et al. 2019). Otsuka et al. (2012) suggested that the plasma motion of MSTIDs can cause the disappearance of the EPBs by transporting the ambient plasma into the plasma-depleted region across the geomagnetic field lines via **E** × **B** drifts. However, the EPBs usually cause significant plasma depletions over 10 TECu (e.g., Nishioka et al. 2008) while the amplitudes of MSTIDs are within the ranges of ~0.2 - 1 TECu (e.g., Tsugawa et al. 2007; Chou et al. 2017), making it difficult to fade out the EPBs by filling the plasma depletions up with ambient plasma along the flux tubes. Additionally, plasma diffusion across the geomagnetic field line is relatively slow compared to the field-aligned diffusion and may take a longer time to fill the depletion up.

To understand how MSTIDs affect the electrodynamics of EPBs, we use the Naval Research Laboratory (NRL) SAMI3/ESF (Sami3 is Also a Model of the Ionosphere/Equatorial Spread F) model (Huba et al. 2008) to investigate the coupling between the nighttime MSTIDs and EPBs. We found that the **E** × **B** drifts within MSTIDs can suppress the upward motion of EPBs and affect the morphology of EPBs. However, the meridional winds also play an essential role in the disappearance of EPBs. Concerning the observations reported by Otsuka et al. (2012) and Shiokawa et al. (2015), both MSTIDs and transequatorial winds appear to be necessary conditions to explain the disappearance of EPBs.

2. THE SAMI3/ESF MODEL

The NRL self-consistent SAMI3/ESF model based on the 2-D SAMI2 (Sami2 is Another Model of the Ionosphere) and 3-D SAMI3 (Huba et al. 2000; Huba and Joyce 2010) has applied to study the evolution and generation of ESF (Huba et al. 2008, 2009a; Krall et al. 2013; Wu et al. 2015) and nighttime MSTIDs (Duly et al. 2014; Chou et al. 2018). In this study, the SAMI2 model is run for 43 h to initiate the SAMI3/ESF model. The geophysical indices used are F10.7 = 105 (s.f.u), F10.7A = 105 (s.f.u), Ap = 37, and day-of-year = 70. The SAMI3/ESF model uses a grid (nz, nf, nl) = (101, 200, 128) where nz is the number of grid points along each geomagnetic field line (s direction, the coordinate along the field line), nf is the number of geomagnetic field lines in altitude (p direction, the coordinate orthogonal to s in the radial direction), and nl is the number in longitude (ϕ direction, the magnetic longitude). Since the 3D model uses an aligned diploe magnetic field with a magnetic apex height from 85 to 2400 km, the geomagnetic latitude and geographic latitude are the same, and the longitudinal and latitudinal width are limited to 4° and ±30° in both hemispheres. The simulations are run for 7 h from ~19:09 LT to ~2:07 LT.

The SAMI3/ESF potential equation is solved based on current conservation $\nabla \cdot J = 0$ and equipotential field lines (Krall et al. 2009a; Kuo et al. 2011; Huba et al. 2015). The electric current J can be written as $J = J_E + J_g + J_v$, where J_E, J_g, and J_v represent current terms driven by the electric field, gravity, and neutral wind. In this study, the external MSTID current terms (J_{MSTID}) are included in the potential equation $\left[\nabla \cdot J = \nabla \cdot (J_E + J_g + J_v + J_{MSTID}) = 0\right]$ to act as the source term for generating MSTIDs. The modified integrated potential equation used in this study is

$$\frac{\partial}{\partial p} p \sum_{pp} \frac{\partial \Phi}{\partial p} - \frac{\partial}{\partial p} \sum_{H} \frac{\partial \Phi}{\partial \phi} + \frac{\partial}{\partial \phi} \frac{1}{p} \sum_{p\phi} \frac{\partial \Phi}{\partial \phi} + \frac{\partial}{\partial \phi} \sum_{H} \frac{\partial \Phi}{\partial p} = \frac{\partial F_{\phi g}}{\partial \phi} + \frac{\partial F_{\phi V}}{\partial \phi} - \frac{\partial F_{pg}}{\partial p} + \frac{\partial F_{pV}}{\partial p} + \frac{\partial F_{pE}}{\partial p} + \frac{\partial F_{\phi E}}{\partial \phi} \quad (1)$$

where $F_{\phi g} = \int (r_E \sin^3\theta/\Delta)(B_0/c)\sigma_{Hc} g_p ds$, $F_{\phi V} = \int (r_E \sin^3\theta/\Delta)(B_0/c)(\sigma_H V_{n\phi} - \sigma_P V_{np})\, ds$, $F_{pg} = -\int r \sin\theta (B_0/c)\sigma_{Pc} g_p ds$, and $F_{pV} = \int r \sin\theta (B_0/c)(\sigma_P V_{n\phi} + \sigma_H V_{np}) ds$, Φ is the electrostatic potential, g_p is the component of gravity perpendicular to B, V_n is perpendicular wind component. The detailed definitions of the variables are given by Huba and Joyce (2010). The MSTID current terms are $F_{\phi E} = \int r^3/r_E^3 (\sin^3\theta/\Delta^2)(\sigma_P E_\phi + \sigma_H E_p)\, ds$ and $F_{pE} = \int r \sin\theta/\Delta (r/r_E)^3 (\sigma_p E_p - \sigma_H E_\phi) ds$, where E_p and E_ϕ are defined as

$$E_{[p,\,\phi]} = -A_E \frac{1}{1 + e^{-(lat - lat_0)}} e^{-\frac{(lon - lon_0)^2}{2w^2}} \frac{k_{[x,\,y]}}{k} \sin(k_x x + k_y y - \omega t) \quad (2)$$

where A_E is the amplitude of electric field, $k_x = k\cos\theta_{TID}$, $k_y = k\sin\theta_{TID}$, $\omega = \frac{2\pi}{T}$, t is time, k is the wavenumber, *lon* and *lat* are longitude and latitude, and θ_{TID} is the angle between the direction normal to the frontal structure of MSTIDs and the geomagnetic east. We assume $k = \frac{2\pi}{2^\circ}$, $\theta_{TID} = 30°$ and T = 70 min, which are similar to the MSTIDs observations (e.g., Shiokawa et al. 2003b). The A_E is set to 2 mV m^{-1} (cf. Pfaff et al. 2005). The smooth function $\frac{1}{1 + e^{-(lat - lat_0)}} e^{-\frac{(lon - lon_0)^2}{2 \times w^2}}$ is used to limit the latitudinal and longitudinal extension of

current oscillations. w, lat_0, and lon_0 are set to 1.25°, 17°, and 2°, respectively, so that the currents will gradually decrease to zero below 17°N at 85 km, and the boundary effect will be reduced. The MSTID current terms are confined to the altitudes of 85 - 450 km in the northern hemisphere and will self-consistently generate polarization electric fields ($E = -\nabla\Phi$) along the field lines to satisfy assumptions of $\nabla \cdot J = 0$ and equipotential field line, leading to a conjugate effect (e.g., Saito et al. 1995; Otsuka et al. 2004).

Similar methods were used by Kuo et al. (2011) and Huba et al. (2015). Huba et al. (2015) simulated the tsunami-induced gravity waves by imposing neutral wind perturbations (U') in the ionospheric F region. The dynamo currents driven by wind perturbations self-consistently induce polarization electric fields mapping to the conjugate region. Kuo et al. (2011) studied the lithosphere-atmosphere-ionosphere coupling by imposed an external dynamo current from the atmosphere at 85 km altitude (the lower boundary for the SAMI3 ionosphere). The dynamo current flowing into the ionosphere causes significant ionospheric perturbations in both hemispheres and EPB formation.

The EPBs are simulated by imposing a Gaussian perturbation in the ion density with an amplitude A_m of 10% in the bottomside F layer.

$$N' = N_0\left[1 - A_m e^{-\frac{(lon - lon_0)^2}{2w^2}}\right] \quad (3)$$

where N_0 and N' are the initial and perturbed ion densities. The perturbation is centered at $lon_0 = 2°$, and $w = 0.3°$. The gravity-driven current terms (F_{pg}, $F_{\phi g}$) of Eq. (1) are the primary source terms to drive the growth of EPBs.

3. RESULTS

Three SAMI3/ESF numerical simulations are performed using zero neutral wind conditions. The neutral winds are not considered here because we want to focus on the first order effects of the MSTIDs on the EPBs. Case 1 simulates the generation and evolution of EPB; cases 2 and 3 simulate the impacts of MSTIDs on the EPBs in the onset and structure phases by imposing synthetic MSTIDs at 22:00 LT and 23:30 LT, respectively. The onset phase demonstrates that the EPBs develop from the crest of upwellings and continuously grow upward and poleward; the structure phase demonstrates that the EPBs are well-developed and will become fossil (e.g., Tsunoda 2015).

Figure 1 shows the time sequence of electron density contours and vertical **E** × **B** drifts in contour lines (black and white lines) as a function of longitude and altitude on a magnetic equatorial plane for cases 1 (left column), 2 (middle column), and 3 (right column), respectively (see also movies in supporting information). The black and white contour lines indicate the downward and upward **E** × **B** drifts, respectively. The yellow and red stars indicate the positions of peak upward **E** × **B** drifts of the EPB and topside EPB (> 900 km). Dense white contour lines within the plume structures are visible, demonstrating strong upward **E** × **B** drifts within the EPB. The EPB starts to grow from the bottomside ionosphere after ~22:00 LT. Case 1 shows that the EPB intrudes into ~1200 km altitude at 01:49 LT, displaying a distinct plume structure. Bifurcations can be identified along the west wall of the plume. The morphology of EPB resembles the turbulent bubble structures shown in Fig. 2 of Yokoyama et al. (2014). The EPB in the onset phase has a peak upward **E** × **B** drift of ~686 m s^{-1} in the F region at 22:47 LT and eventually decrease to 364 m s^{-1} in the structure phase at 01:49 LT. The topside EPB above 900 km has weaker peak vertical drifts ranging from 136 to 156 m s^{-1}.

It is noteworthy that EPBs usually occur during ~19:00 - 20:00 LT because the PRE can accelerate the growth rate. The simulated EPBs develop after 22:00 LT are due to the background conditions (e.g., Sultan 1996). SAMI3/ESF uses the empirical thermosphere models NRLMSIS00 (Picone et al. 2002) to specify the neutral species. The background conditions may be different from the real situation, which in turn affect the growth rate (e.g., Huba and Liu 2020). However, EPBs could occur after 22:00 LT in June solstice (Yizengaw et al. 2013; Ajith et al. 2015, 2016), making the MSTIDs that often occur after 21:00 LT around solstice to have a higher probability of encountering the EPBs. Nevertheless, the onset time of EPBs will not affect the electrodynamics between the EPBs and MSTIDs.

In case 2, ionospheric undulations due to the MSTIDs are discernible in the topside ionosphere. The MSTIDs have vertical **E** × **B** drifts of ~±10 - 50 m s^{-1}, which agrees reasonably well with the MSTIDs observations (e.g., Shiokawa et al. 2003b). While the MSTIDs encounter the EPB in the onset phase, the MSTIDs suppress the EPB growth and eventually confine the EPB within ~1100 km altitude at 01:49 LT. The peak upward **E** × **B** drifts of the topside EPB decrease to ~122 m s^{-1} while encountering the downward **E** × **B** drifts of MSTIDs at 23:48 LT. Bifurcations on the east wall of the plume are suppressed as well. However, the upward **E** × **B** drifts of MSTIDs also favor the growth of EPB at 00:48 and 01:49 LT, leading to the increase of peak upward **E** × **B** drifts within the topside EPB. Of particular interest is that the MSTIDs affect the morphology of EPB. The EPB stretches along with the band structure of MSTIDs, displaying a reverse C shape of EPB. In case 3, the MSTIDs also distort and suppress the EPB in the structure phase. The primary plume is confined within ~1100 km altitude, and the upward **E** × **B** drifts of topside EPB decrease to ~91 m s^{-1} at 01:49 LT. In general, the peak upward **E** × **B** drifts of the bottomside EPBs are similar for three cases; however, the MSTIDs significantly impact the morphology of EPBs above the F region in the onset and structure

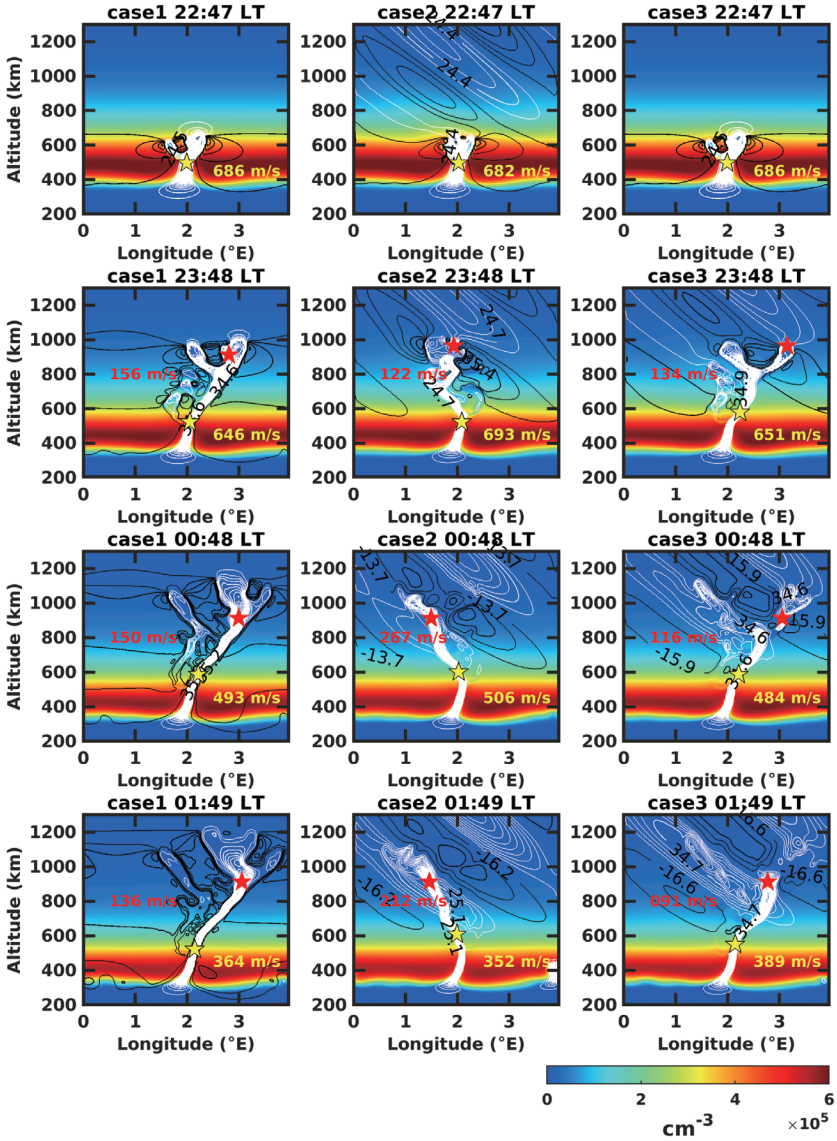

Fig. 1. The time sequence of electron density contours as a function of longitude and altitude at 22:47 LT, 23:48 LT, 00:48 LT, and 01:49 LT for case 1 (left column), case 2 (middle column), and case 3 (right column). The black and white contour lines indicate the downward and upward **E** × **B** drifts, respectively. The yellow and red stars indicate the positions of peak upward **E** × **B** drifts of the EPB and topside EPB (> 900 km). Case 1 simulates the EPB without the MSTIDs. Cases 2 and 3 simulate the interaction between the EPB and MSTIDs at 22:30 LT and 23:30 LT, respectively.

phases. Note the MSTIDs only occur above 600 km altitudes on the magnetic equatorial plane because MSTIDs are electrodynamic structures in the midlatitude, which could induce polarization electric fields mapping along the field line to the conjugate hemisphere, leading to ionospheric perturbations along the field line.

We further calculate the OI 630-nm airglow emission rate based on Sobral et al. (1993) to compare with Otsuka et al. (2012). Figure 2 shows the time sequence of the airglow intensity deviation maps at 250 km altitude as a function of longitude and latitude for cases 1 (left column), 2 (middle column), and 3 (right column). Additional movie files show this in more detail (see movies in supporting information). The airglow intensity deviation (I_p) is defined as $I_p = (I - I_c)/I_c$, where I_c is the control run without EPBs, and I is the OI 630-nm airglow emission rate for cases 1 - 3. Note that the background airglow intensity deviation can reach over 20%; we limit the colorbar ranges between -1% and 2% to highlight the EPB variations. Case 1 shows the evolution of EPB with airglow depletion. The EPB extends to about 21°N at 01:49 LT. MSTIDs can be identified with airglow enhancements and depletions above 13°N in cases 2 and 3. Cases 2 and 3 show that MSTIDs affect the latitudinal extent and morphology of EPB, confining the EPB within 21°N. However, the EPB is still distinct, implying that MSTIDs alone are insufficient to explain the disappearance of EPBs.

Otsuka et al. (2012) showed an increase of OI 630-nm airglow deviations while the EPB encountered the MSTIDs.

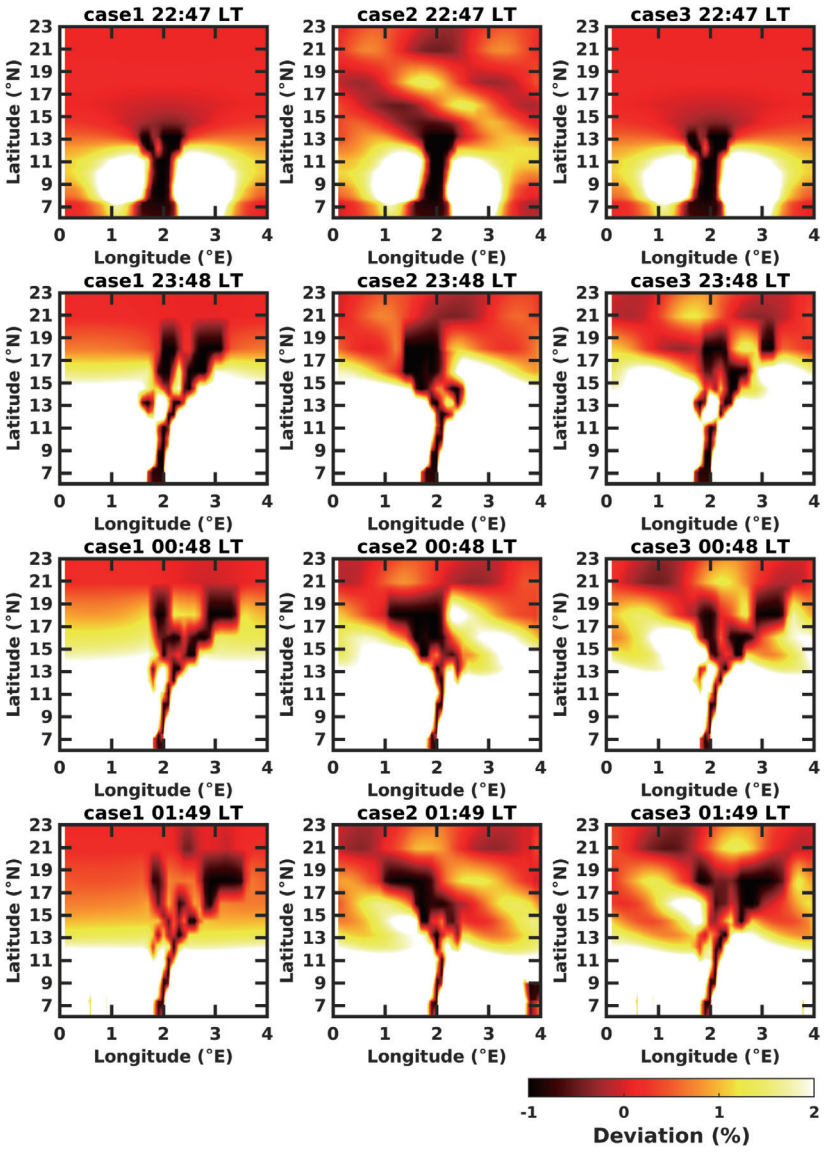

Fig. 2. The time sequence of airglow intensity perturbations as a function of longitude and latitude at 22:47 LT, 23:48 LT, 00:48 LT, and 01:49 LT for case 1 (first column), case 2 (second column), and case 3 (third column).

Shiokawa et al. (2015) also showed clearly airglow intensity decrease at Darwin, Australia, and a slight increase at Sata, Japan, while the EPB encountered the TIDs at geomagnetically conjugate points. The sudden F-layer rise (descent) can cause a decrease (increase) of the 630-nm airglow intensity because the 630-nm airglow intensity is proportional to the O^+ and O_2 density, and rising (descending) F-layer will encounter decreasing (increasing) ambient O_2 density. The airglow intensity enhancement implies that the transequatorial wind may contribute to the disappearance of EPBs.

To further understand the transequatorial wind effects on the disappearance of EPB, we focus on the EPBs in the structure phase and incorporate the southward winds V = -60tan$h$[0.02 × (*altitude* - 100)] m s^{-1} into cases 1 and 3 at 23:30 LT, referred to as cases 4 and 5. The southward winds can reach a peak of 60 m s^{-1} above 250 km and are assumed to be 0 m s^{-1} under 100 km. Figure 3 is the same as Fig. 2 but for case 4 (top panel) and case 5 (bottom panel) in both hemispheres. Additional movie files show this in more detail (see movies in supporting information). Transparent meridionally-elongated wedges of airglow depletions related to EPBs are visible in both cases. Significant airglow enhancements on either side of EPBs are visible due to the downward **E** × **B** drifts outside the EPBs pushing the plasma downward. In case 4, the airglow deviations of EPB in the northern hemisphere significantly become less evident compared to the EPB in the southern hemisphere, displaying a hemispheric asymmetry of EPB. However, the EPB is still distinct in both hemispheres, suggesting that meridional wind alone is insufficient to fade the EPB out. In case

5, it shows that the EPB is almost evanescent in the northern hemisphere while interacting with the MSTIDs. Simulations reveal that both MSTIDs and meridional wind are likely necessary to comprehend the disappearance of EPB.

4. DISCUSSION

Otsuka et al. (2012) and Shiokawa et al. (2015) suggested that MSTIDs can fill the EPBs up by transporting plasma into the depletions via **E** × **B** drifts. In our simulations, we found that MSTIDs can suppress the upward motion of EPBs; however, MSTIDs alone are insufficient to explain the disappearance of EPBs. The meridional winds should be included in the processes to explain the disappearance of EPBs in the airglow observations adequately. These processes involve (1) the suppression of upward **E** × **B** drifts within the EPBs, (2) the decrease in background electron density, (3) and the transport of ambient plasma by MSTIDs.

First, the suppression of upward **E** × **B** drifts occurred when EPBs interact with MSTIDs and meridional winds. Figure 4 shows the local time variations of peak vertical **E** × **B** drifts of the topside EPBs for cases 1 - 5. Cases 2 and 3 show significant fluctuations due to the interactions of upward and downward **E** × **B** drifts within the MSTIDs. The MSTIDs can suppress or aid the upward motion of EPBs by reducing or increasing the upward **E** × **B** drifts in comparison with case 1. When the southward winds are applied, cases 4 and 5 show that the southward winds can significantly suppress the EPBs by reducing the vertical **E** × **B** drifts to ~250 m s^{-1}. Krall et al. (2009b) and Huba and Krall (2013) suggested that a uniform meridional wind perpendicular to the magnetic field has a direct stabilizing effect on EPB development. The meridional wind parallel to the magnetic field can also indirectly stabilize the EPBs by altering the Pedersen conductivity. Figure 5 shows the distributions of Pedersen conductivity (top), electron density (middle), and vertical **E** × **B** drift (bottom) as a function of latitude and altitude in 2°E for case 1 (left), case 4 (middle), and case 5 (right) at 01:49 LT. In comparison with case 1, case 4 shows that the Pedersen conductivity is decreased (increased) when the southward winds move the plasma to higher (lower) altitudes in the northern (southern) hemisphere. The increase of electron density in the bottomside ionosphere will lead to the increase of field-line integrated Pedersen conductivity since the Pedersen conductivity is proportional to electron and neutral densities (Kelley 1989). The ionospheric E region with increased Pedersen conductivity would short out the polarization electric fields within the EPB, which, in turn, suppress the EPB growth (e.g., Huba et al. 2020). Case 5 also shows that the MSTIDs can increase (decrease) the Pedersen conductivity in the bottomside ionosphere (below 300 km) by transporting the plasma to lower (higher) altitude via downward (upward) **E** × **B** drifts, which is consistent with the Perkins instability.

Second, the meridional winds significantly reduce the background electron density and airglow intensity. Figure 5 (middle) shows that the southward winds move the plasma upward (downward) in the northern (southern) hemisphere, leading to a decrease (increase) of plasma density in the bottomside ionosphere (below 350 km altitude). Since the OI 630-nm airglow emission rate peaks at ~250 km, the decrease of electron density at ~250 km could lead to the decrease of airglow intensity. The top panel of Fig. 3 also shows that the EPBs in both hemispheres are asymmetric. The relative airglow deviations of EPB become smaller in the northern hemisphere, demonstrating that the decrease in plasma density and airglow intensity would make EPB inconspicuous, providing conditions favorable for MSTIDs to fade out the EPBs.

Third, MSTIDs can efficiently fade the EPBs out when the upward **E** × **B** drifts within the EPBs and background electron density are reduced. The decrease of background electron density also leads to a decrease of upward **E** × **B** drifts within the EPBs (e.g., Krall et al. 2010). Then, the MSTIDs move plasma downward to fill the EPB depletions up via **E** × **B** drifts, which, in turn, lead to the enhancement of the 630-nm airglow intensity (bottom panel of Fig. 3). Our simulated OI 630-nm results essentially agree with the airglow observations reported by Otsuka et al. (2012) and Shiokawa et al. (2015). It should be mentioned that Otsuka et al. (2012) showed that the EPB is nearly the fossil state when encountering the MSTIDs, implying that the upward **E** × **B** drifts within the EPB should be weak. The MSTIDs and meridional winds should be more efficiently suppressing the EPB.

Although the meridional winds and MSTIDs contribute to the disappearance of EPBs in the OI 630-nm airglow observations, distinct depletions in Pedersen conductivity and electron density above ~300 km are still visible in the equatorial ionosphere (Fig. 5, case 5), suggesting that the EPBs still persist due to abundant background electron density in the F region. This can explain why strong spread-F still present in ionograms when the EPBs were disappeared in the airglow images (Shiokawa et al. 2015).

On the other hand, we found that MSTIDs can lead to west-tilted EPBs due to its wavefront orientation. The west-tilted EPBs are usually considered to be related to the latitudinal variation of eastward plasma flow due to zonal wind (Kelley et al. 2003; Huba et al. 2009b). The eastward plasma flow peaks at the equatorial region can lead to a reverse C- or arc-shape EPBs (Kil et al. 2009). Figure 6 shows the variations of zonal **E** × **B** drifts as a function of longitude and altitude for cases 1 (top panel) and 2 (bottom panel). In case 1, the primary plume tilts eastward due to the eastward **E** × **B** drifts within the EPB. The bifurcations on the west wall of the plume can be identified with the westward **E** × **B** drifts. In case 2, the primary plume initially grows eastward due to the eastward **E** × **B** drifts within the EPB (Fig. 6e).

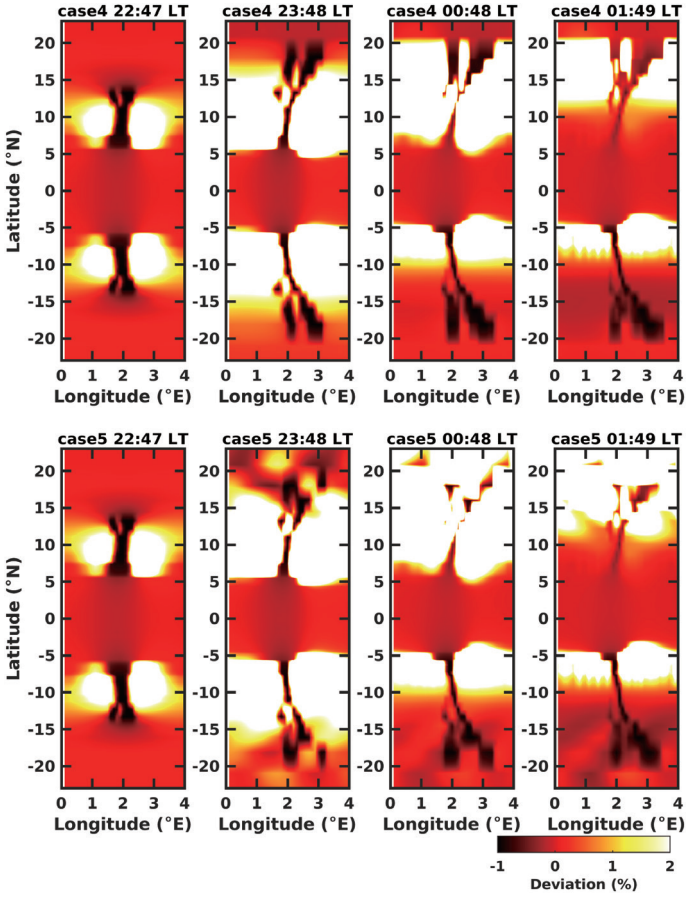

Fig. 3. The time sequence of airglow intensity perturbations as a function of longitude and latitude at 22:48 LT, 23:48 LT, 00:48 LT, and 01:48 LT for case 4 (top panel) and case 5 (bottom panel).

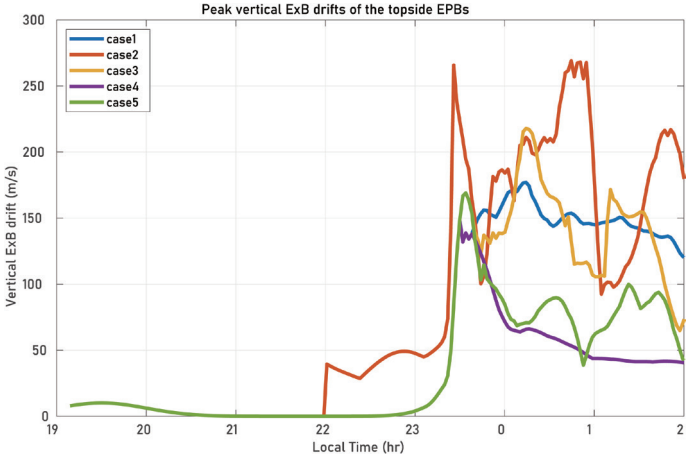

Fig. 4. The peak vertical **E** × **B** drift variations of the topside EPBs (> 900 km) as a function of time for cases 1 - 5.

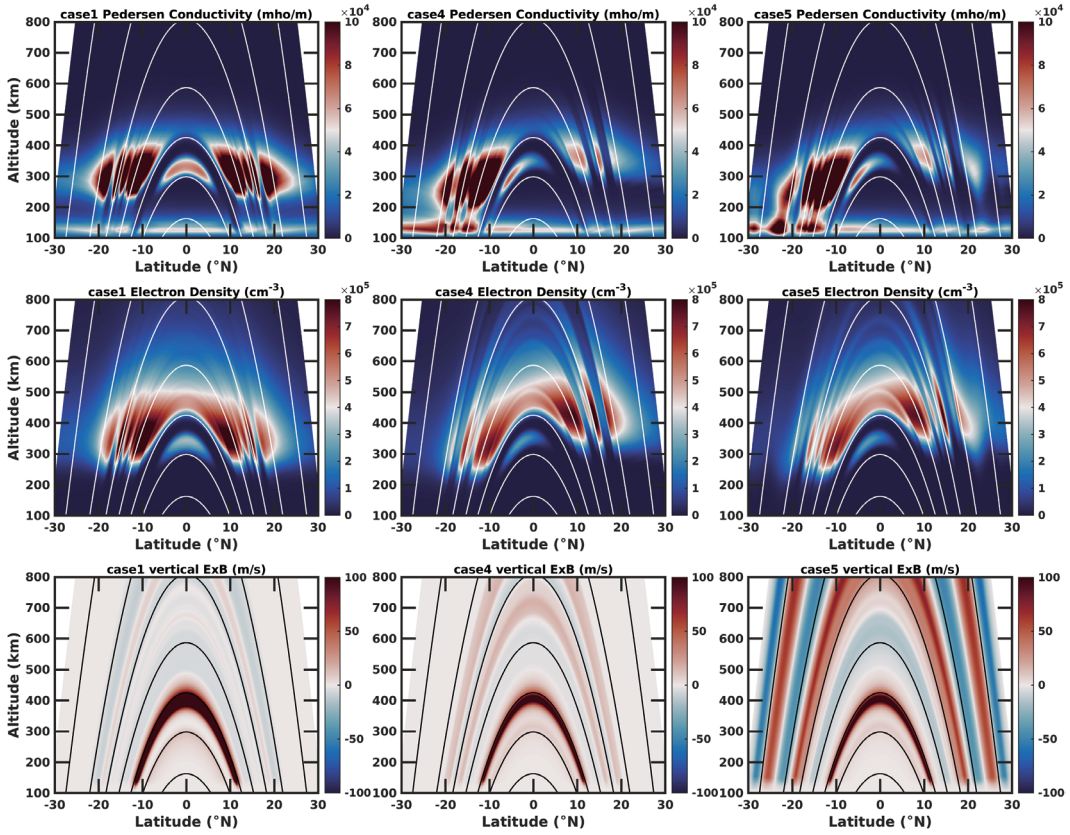

Fig. 5. The Pedersen conductivity (top row), electron density (middle row), and vertical **E** × **B** drift (bottom row) contours as a function of latitude and altitude in ~2°E at 01:49 LT for case 1 (left column), case 4 (middle column), and case 5 (right column). The white (top and middle rows) and black lines (bottom row) indicate the geomagnetic field line.

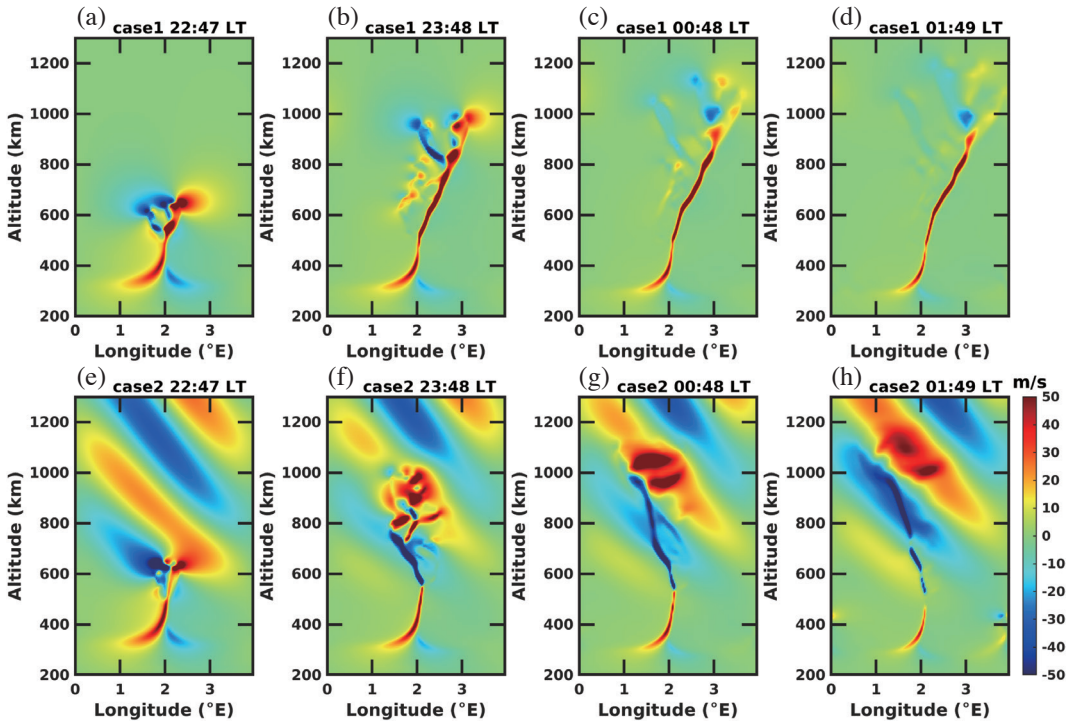

Fig. 6. The time sequence of zonal **E** × **B** drift contours as a function of longitude and altitude at 22:47 LT, 23:48 LT, 00:48 LT, and 01:49 LT for cases 1 (top row) and 2 (bottom row). The positive and negative values indicate eastward and westward **E** × **B** drifts, respectively.

As the EPB grows upward and encounters the MSTIDs with westward **E** × **B** drifts, the primary plume turns westward and stretches along with the band structure of MSTIDs (Figs. 6f - h). The bifurcations on the east wall of the plume grow eastward while encountering the MSTIDs with eastward **E** × **B** drifts. However, they are suppressed by the downward **E** × **B** drifts of MSTIDs as shown in Fig. 1. A similar phenomenon was observed by Aa et al. (2019) that they found the EPBs merged and stretched along with the mid-latitude TIDs.

5. CONCLUSION

We study the interaction between the equatorial EPBs and mid-latitude nighttime MSTIDs with the SAMI3/ESF model. Simulations reveal that MSTIDs alone can affect the morphology of EPBs; however, MSTIDs are insufficient to explain the disappearance of EPBs. The inclusion of meridional winds is necessary to comprehend the underlying mechanism of EPB disappearance. Both MSTIDs and meridional winds can suppress the upward **E** × **B** drifts within the EPBs and reduce the background electron density, providing conditions favorable for the MSTIDs to fill the plasma depletion up through **E** × **B** drifts. Besides, the vertical and zonal **E** × **B** drifts within the MSTIDs can significantly affect the morphology of EPBs in the onset phase, making EPBs stretch along with the band structure of MSTIDs, which in turn result in a reverse C-shape EPB. This study provides a new theoretical aspect of the interaction when the equatorial ionospheric irregularities meet the mid-latitude irregularities.

Acknowledgements This study is supported by the Taiwan Ministry of Science and Technology under MOST-108-2638-M-006-001-MY2. MYC is supported by National Science Foundation grant AGS-1522830. JDH was supported by NASA grant NNH17ZDA001N and National Science Foundation grant AGS-1931415.

REFERENCES

Aa, E., S. Zou, A. Ridley, S. Zhang, A. J. Coster, P. J. Erickson, S. Liu, and J. Ren, 2019: Merging of storm time midlatitude traveling ionospheric disturbances and equatorial plasma bubbles. *Space Weather*, **17**, 285-298, doi: 10.1029/2018SW002101. [Link]

Abdu, M. A., E. Alam Kherani, I. S. Batista, E. R. de Paula, D. C. Fritts, and J. H. A. Sobral, 2009: Gravity wave initiation of equatorial spread F/plasma bubble irregularities based on observational data from the SpreadFEx campaign. *Ann. Geophys.*, **27**, 2607-2622, doi: 10.5194/angeo-27-2607-2009. [Link]

Ajith, K. K., S. T. Ram, M. Yamamoto, T. Yokoyama, V. S. Gowtam, Y. Otsuka, T. Tsugawa, and K. Niranjan, 2015: Explicit characteristics of evolutionary-type plasma bubbles observed from Equatorial Atmosphere Radar during the low to moderate solar activity years 2010-2012. *J. Geophys. Res.*, **120**, 1371-1382, doi: 10.1002/2014JA020878. [Link]

Ajith, K. K., S. Tulasi Ram, M. Yamamoto, Y. Otsuka, and K. Niranjan, 2016: On the fresh development of equatorial plasma bubbles around the midnight hours of June solstice. *J. Geophys. Res.*, **121**, 9051-9062, doi: 10.1002/2016JA023024. [Link]

Behnke, R., 1979: *F* layer height bands in the nocturnal ionosphere over Arecibo. *J. Geophys. Res.*, **84**, 974-978, doi: 10.1029/JA084iA03p00974. [Link]

Chou, M.-Y., C. C. H. Lin, J. Yue, L. C. Chang, H.-F. Tsai, and C.-H. Chen, 2017: Medium-scale traveling ionospheric disturbances triggered by Super Typhoon Nepartak (2016). *Geophys. Res. Lett.*, **44**, 7569-7577, doi: 10.1002/2017GL073961. [Link]

Chou, M.-Y., C. C. H. Lin, J. D. Huba, C.-P. Lien, C.-H. Chen, J. Yue, L. C. Chang, and P. K. Rajesh, 2018: Numerical modeling of the concentric gravity wave seeding of low-latitude nighttime medium-scale traveling ionospheric disturbances. *Geophys. Res. Lett.*, **45**, 6390-6399, doi: 10.1029/2018GL077959. [Link]

Cosgrove, R. B. and R. T. Tsunoda, 2004: Instability of the *E-F* coupled nighttime midlatitude ionosphere. *J. Geophys. Res.*, **109**, A04305, doi: 10.1029/2003JA010243. [Link]

Duly, T. M., J. D. Huba, and J. J. Makela, 2014: Self-consistent generation of MSTIDs within the SAMI3 numerical model. *J. Geophys. Res.*, **119**, 6745-6757, doi: 10.1002/2014JA020146. [Link]

Dungey, J. W., 1956: Convective diffusion in the equatorial *F* region. *J. Atmos. Terr. Phys.*, **9**, 304-310, doi: 10.1016/0021-9169(56)90148-9. [Link]

Huang, C.-S., C. A. Miller, and M. C. Kelley, 1994: Basic properties and gravity wave initiation of the midlatitudeFregion instability. *Radio Sci.*, **29**, 395-405, doi: 10.1029/93RS01669. [Link]

Huba, J. D. and G. Joyce, 2010: Global modeling of equatorial plasma bubbles. *Geophys. Res. Lett.*, **37**, L17104, doi: 10.1029/2010GL044281. [Link]

Huba, J. D. and J. Krall, 2013: Impact of meridional winds on equatorial spread *F*: Revisited. *Geophys. Res. Lett.*, **40**, 1268-1272, doi: 10.1002/grl.50292. [Link]

Huba, J. D. and H.-L. Liu, 2020: Global modeling of equatorial spread *F* with SAMI3/WACCM-X. *Geophys. Res. Lett.*, **47**, e2020GL088258, doi: 10.1029/2020GL088258. [Link]

Huba, J. D., G. Joyce, and J. A. Fedder, 2000: Sami2 is Another Model of the Ionosphere (SAMI2): A new low-latitude ionosphere model. *J. Geophys. Res.*, **105**, 23035-23053, doi: 10.1029/2000ja000035. [Link]

Huba, J. D., G. Joyce, and J. Krall, 2008: Three-dimensional

equatorial spread *F* modeling. *Geophys. Res. Lett.*, **35**, L10102, doi: 10.1029/2008GL033509. [Link]

Huba, J. D., G. Joyce, J. Krall, and J. Fedder, 2009a: Ion and electron temperature evolution during equatorial spread *F*. *Geophys. Res. Lett.*, **36**, L15102, doi: 10.1029/2009GL038872. [Link]

Huba, J. D., S. L. Ossakow, G. Joyce, J. Krall, and S. L. England, 2009b: Three-dimensional equatorial spread *F* modeling: Zonal neutral wind effects. *Geophys. Res. Lett.*, **36**, L19106, doi: 10.1029/2009GL040284. [Link]

Huba, J. D., D. P. Drob, T.-W. Wu, and J. J. Makela, 2015: Modeling the ionospheric impact of tsunami-driven gravity waves with SAMI3: Conjugate effects. *Geophys. Res. Lett.*, **42**, 5719-5726, doi: 10.1002/2015GL064871. [Link]

Huba, J. D., J. Krall, and D. Drob, 2020: Modeling the impact of metallic ion layers on equatorial spread with SAMI3/ESF. *Geophys. Res. Lett.*, **47**, e2020GL087224, doi: 10.1029/2020GL087224. [Link]

Kelley, M. C., 1989: The Earth's Ionosphere: Plasma Physics and Electrodynamics, Academic Press, San Diego, CA, 487 pp, doi: 10.1016/B978-0-12-404013-7.X5001-1. [Link]

Kelley, M. C. and S. Fukao, 1991: Turbulent upwelling of the mid-latitude ionosphere: 2. Theoretical framework. *J. Geophys. Res.*, **96**, 3747-3753, doi: 10.1029/90JA02252. [Link]

Kelley, M. C., J. J. Makela, A. Saito, N. Aponte, M. Sulzer, and S. A. González, 2000: On the electrical structure of airglow depletion/height layer bands over Arecibo. *Geophys. Res. Lett.*, **27**, 2837-2840, doi: 10.1029/2000gl000024. [Link]

Kelley, M. C., J. J. Makela, L. J. Paxton, F. Kamalabadi, J. M. Comberiate, and H. Kil, 2003: The first coordinated ground- and space-based optical observations of equatorial plasma bubbles. *Geophys. Res. Lett.*, **30**, 1766, doi: 10.1029/2003GL017301. [Link]

Kil, H., R. A. Heelis, L. J. Paxton, and S.-J. Oh, 2009: Formation of a plasma depletion shell in the equatorial ionosphere. *J. Geophys. Res.*, **114**, A11302, doi: 10.1029/2009JA014369. [Link]

Krall, J., J. D. Huba, and C. R. Martinis, 2009a: Three-dimensional modeling of equatorial spread *F* airglow enhancements. *Geophys. Res. Lett.*, **36**, L10103, doi: 10.1029/2009GL038441. [Link]

Krall, J., J. D. Huba, G. Joyce, and S. T. Zalesak, 2009b: Three-dimensional simulation of equatorial spread-F with meridional wind effects. *Ann. Geophys.*, **27**, 1821-1830, doi: 10.5194/angeo-27-1821-2009. [Link]

Krall, J., J. D. Huba, S. L. Ossakow, and G. Joyce, 2010: Why do equatorial ionospheric bubbles stop rising? *Geophys. Res. Lett.*, **37**, L09105, doi: 10.1029/2010GL043128. [Link]

Krall, J., J. D. Huba, S. L. Ossakow, G. Joyce, J. J. Makela, E. S. Miller, and M. C. Kelley, 2011: Modeling of equatorial plasma bubbles triggered by non-equatorial traveling ionospheric disturbances. *Geophys. Res. Lett.*, **38**, L08103, doi: 10.1029/2011GL046890. [Link]

Krall, J., J. D. Huba, G. Joyce, and M. Hei, 2013: Simulation of the seeding of equatorial spread *F* by circular gravity waves. *Geophys. Res. Lett.*, **40**, 1-5, doi: 10.1029/2012GL054022. [Link]

Kuo, C. L., J. D. Huba, G. Joyce, and L. C. Lee, 2011: Ionosphere plasma bubbles and density variations induced by pre-earthquake rock currents and associated surface charges. *J. Geophys. Res.*, **116**, A10317, doi: 10.1029/2011JA016628. [Link]

Li, G., Y. Otsuka, B. Ning, M. A. Abdu, M. Yamamoto, W. Wan, L. Liu, and P. Abadi, 2016: Enhanced ionospheric plasma bubble generation in more active ITCZ. *Geophys. Res. Lett.*, **43**, 2389-2395, doi: 10.1002/2016GL068145. [Link]

Miller, C. A., W. E. Swartz, M. C. Kelley, M. Mendillo, D. Nottingham, J. Scali, and B. Reinisch, 1997: Electrodynamics of midlatitude spread *F*: 1. Observations of unstable, gravity wave-induced ionospheric electric fields at tropical latitudes. *J. Geophys. Res.*, **102**, 11521-11532, doi: 10.1029/96JA03839. [Link]

Miller, E. S., J. J. Makela, and M. C. Kelley, 2009: Seeding of equatorial plasma depletions by polarization electric fields from middle latitudes: Experimental evidence. *Geophys. Res. Lett.*, **36**, L18105, doi: 10.1029/2009GL039695. [Link]

Nishioka, M., A. Saito, and T. Tsugawa, 2008: Occurrence characteristics of plasma bubble derived from global ground-based GPS receiver networks. *J. Geophys. Res.*, **113**, A05301, doi: 10.1029/2007JA012605. [Link]

Ogawa, T., E. Sagawa, Y. Otsuka, K. Shiokawa, T. I. Immel, S. B. Mende, and P. Wilkinson, 2005: Simultaneous ground- and satellite-based airglow observations of geomagnetic conjugate plasma bubbles in the equatorial anomaly. *Earth Planets Space*, **57**, 385-392, doi: 10.1186/bf03351822. [Link]

Otsuka, Y., K. Shiokawa, T. Ogawa, and P. Wilkinson, 2002: Geomagnetic conjugate observations of equatorial airglow depletions. *Geophys. Res. Lett.*, **29**, 43-1-43-4, doi: 10.1029/2002GL015347. [Link]

Otsuka, Y., K. Shiokawa, T. Ogawa, and P. Wilkinson, 2004: Geomagnetic conjugate observations of medium-scale traveling ionospheric disturbances at midlatitude using all-sky airglow imagers. *Geophys. Res. Lett.*, **31**, L15803, doi: 10.1029/2004GL020262. [Link]

Otsuka, Y., K. Shiokawa, and T. Ogawa, 2012: Disappearance of equatorial plasma bubble after interaction with mid-latitude medium-scale traveling ionospheric disturbance. *Geophys. Res. Lett.*, **39**, L14105, doi: 10.1029/2012GL052286. [Link]

Perkins, F., 1973: Spread *F* and ionospheric currents. *J. Geophys. Res.*, **78**, 218-226, doi: 10.1029/JA078i001p00218. [Link]

Pfaff, R., H. Freudenreich, T. Yokoyama, M. Yamamoto, S. Fukao, H. Mori, S. Ohtsuki, and N. Iwagami, 2005: Electric field measurements of DC and long wavelength structures associated with sporadic-*E* layers and QP radar echoes. *Ann. Geophys.*, **23**, 2319-2334, doi: 10.5194/angeo-23-2319-2005. [Link]

Picone, J. M., A. E. Hedin, D. P. Drob, and A. C. Aikin, 2002: NRLMSISE-00 empirical model of the atmosphere: Statistical comparisons and scientific issues. *J. Geophys. Res.*, **107**, 1468, doi: 10.1029/2002JA009430. [Link]

Rajesh, P. K., J. Y. Liu, C. H. Lin, A. B. Chen, R. R. Hsu, C. H. Chen, and J. D. Huba, 2016: Space-based imaging of nighttime medium-scale traveling ionospheric disturbances using FORMOSAT-2/ISUAL 630.0 nm airglow observations. *J. Geophys. Res.*, **121**, 4769-4781, doi: 10.1002/2015JA022334. [Link]

Rajesh, P. K., C. H. Lin, C. H. Chen, J. T. Lin, T. Matsuo, M. Y. Chou, W. H. Chen, M. T. Chang, and C. F. You, 2017: Equatorial plasma bubble generation/inhibition during 2015 St. Patrick's Day storm. *Space Weather*, **15**, 1141-1150, doi: 10.1002/2017SW001641. [Link]

Rama Rao, P. V. S., P. T. Jayachandran, and P. S. Ram, 1997: Ionospheric irregularities: The role of the equatorial ionization anomaly. *Radio Sci.*, **32**, 1551-1557, doi: 10.1029/97RS00665. [Link]

Saito, A., T. Iyemori, M. Sugiura, N. C. Maynard, T. L. Aggson, L. H. Brace, M. Takeda, and M. Yamamoto, 1995: Conjugate occurrence of the electric field fluctuations in the nighttime midlatitude ionosphere. *J. Geophys. Res.*, **100**, 21439-21451, doi: 10.1029/95JA01505. [Link]

Saito, A., T. Iyemori, L. G. Blomberg, M. Yamamoto, and M. Takeda, 1998: Conjugate observations of the midlatitude electric field fluctuations with the MU radar and the Freja satellite. *J. Atmos. Sol.-Terr. Phys.*, **60**, 129-140, doi: 10.1016/s1364-6826(97)00094-1. [Link]

Shiokawa, K., C. Ihara, Y. Otsuka, and T. Ogawa, 2003a: Statistical study of nighttime medium-scale traveling ionospheric disturbances using midlatitude airglow images. *J. Geophys. Res.*, **108**, 1052, doi: 10.1029/2002JA009491. [Link]

Shiokawa, K., Y. Otsuka, C. Ihara, T. Ogawa, and F. J. Rich, 2003b: Ground and satellite observations of nighttime medium-scale traveling ionospheric disturbance at midlatitude. *J. Geophys. Res.*, **108**, 1145, doi: 10.1029/2002JA009639. [Link]

Shiokawa, K., Y. Otsuka, K. J. W. Lynn, P. Wilkinson, and T. Tsugawa, 2015: Airglow-imaging observation of plasma bubble disappearance at geomagnetically conjugate points. *Earth Planets Space*, **67**, 43, doi: 10.1186/s40623-015-0202-6. [Link]

Sobral, J. H. A., H. Takahashi, M. A. Abdu, P. Muralikrishna, Y. Sahai, C. J. Zamlutti, E. R. de Paula, and P. P. Batista, 1993: Determination of the quenching rate of the $O(^1D)$ by $O(^3P)$ from rocket-borne optical (630 nm) and electron density data. *J. Geophys. Res.*, **98**, 7791-7798, doi: 10.1029/92JA01839. [Link]

Sultan, P. J., 1996: Linear theory and modeling of the Rayleigh-Taylor instability leading to the occurrence of equatorial spread *F*. *J. Geophys. Res.*, **101**, 26875-26891, doi: 10.1029/96JA00682. [Link]

Takahashi, H., C. M. Wrasse, C. A. O. B. Figueiredo, D. Barros, M. A. Abdu, Y. Otsuka, and K. Shiokawa, 2018: Equatorial plasma bubble seeding by MSTIDs in the ionosphere. *Prog. Earth Planet. Sci.*, **5**, doi: 10.1186/s40645-018-0189-2. [Link]

Tsugawa, T., Y. Otsuka, A. J. Coster, and A. Saito, 2007: Medium-scale traveling ionospheric disturbances detected with dense and wide TEC maps over North America. *Geophys. Res. Lett.*, **34**, L22101, doi: 10.1029/2007GL031663. [Link]

Tsunoda, R. T., 2015: Upwelling: A unit of disturbance in equatorial spread *F*. *Prog. Earth Planet. Sci.*, **2**, 9, doi: 10.1186/s40645-015-0038-5. [Link]

Tsunoda, R. T., R. B. Cosgrove, and T. Ogawa, 2004: Azimuth-dependent E_s layer instability: A missing link found. *J. Geophys. Res.*, **109**, A12303, doi: 10.1029/2004JA010597. [Link]

Tulasi Ram, S., P. V. S. Rama Rao, K. Niranjan, D. S. V. V. D. Prasad, R. Sridharan, C. V. Devasia, and S. Ravindran, 2006: The role of post-sunset vertical drifts at the equator in predicting the onset of VHF scintillations during high and low sunspot activity years. *Ann. Geophys.*, **24**, 1609-1616, doi: 10.5194/angeo-24-1609-2006. [Link]

Tulasi Ram, S., P. V. S. Rama Rao, D. S. V. V. D. Prasad, K. Niranjan, A. Raja Babu, R. Sridharan, and C. V. Devasia, 2007: The combined effects of electrojet strength and the geomagnetic activity (K_p-index) on the post sunset height rise of the F-layer and its role in the generation of ESF during high and low solar activity periods. *Ann. Geophys.*, **25**, 2007-2017, doi: 10.5194/angeo-25-2007-2007. [Link]

Wu, T.-W., J. D. Huba, J. Krall, D. C. Fritts, and B. Laughman, 2015: Seeding equatorial spread *F* with turbulent gravity waves: Phasing effects. *Geophys. Res. Lett.*, **42**, 15-21, doi: 10.1002/2014GL062348. [Link]

Yizengaw, E., J. Retterer, E. E. Pacheco, P. Roddy, K. Groves, R. Caton, and P. Baki, 2013: Postmidnight bubbles and scintillations in the quiet-time June solstice. *Geophys. Res. Lett.*, **40**, 5592-5597, doi: 10.1002/2013GL058307. [Link]

Yokoyama, T., D. L. Hysell, Y. Otsuka, and M. Yamamoto, 2009: Three-dimensional simulation of the coupled

Perkins and Es-layer instabilities in the nighttime mid-latitude ionosphere. *J. Geophys. Res.*, **114**, A03308, doi: 10.1029/2008JA013789. [Link]

Yokoyama, T., H. Shinagawa, and H. Jin, 2014: Nonlinear growth, bifurcation, and pinching of equatorial plasma bubble simulated by three-dimensional high-resolution bubble model. *J. Geophys. Res.*, **119**, 10474-10482, doi: 10.1002/2014JA020708. [Link]